Strain-Insensitive Temperature Sensor Based on Few-Mode Fiber and Photonic Crystal Fiber

Xuekai Gao [ID], Jian Xu [ID], Caijian Xie [ID], Wei Zhang, Li Pei [ID], Jingjing Zheng, Jing Li [ID], and Tigang Ning

Abstract—**Based on few-mode fiber (FMF) and photonic crystal fiber (PCF), a new temperature sensor with a FMF-PCF-FMF hybrid construction has been developed. Furthermore, the sensor has a longitudinally symmetrical structure that makes it have a flexible sensor head, which enhances the practical performance. Simulated results show that there are three resonant peaks with extinction ratio above 18 dB in the wavelength from 1630 nm to 1720 nm, and the temperature can be measured by calculating wavelength shift of resonant peaks. The experimental results show that the temperature sensitivity of the proposed sensor is as high as 38.6 pm/°C when the temperature ranges from 20°C to 80°C. Meanwhile, the strain sensitivity of the proposed sensor is as low as -0.457 pm/$\mu\varepsilon$ when strain ranges from 0 to 3000 $\mu\varepsilon$. The high temperature sensitivity and ultralow strain sensitivity indicate that the proposed sensor can effectively eliminate the cross-sensitive issue of temperature and strain. In addition to excellent sensing performances, simple and compact structure make the proposed sensor be potential in practical applications.**

Index Terms—**Fiber optical sensor, few-mode fiber, photonic crystal fiber.**

I. INTRODUCTION

SENSING technology plays a more and more important role in the development of science and society. Nowadays, sensing technology is widely employed in medical health, industrial, security surveillance, intelligent transportation, and other application fields. Optical fiber sensing technology allows fibers to work as the transmission medium and optical modulator simultaneously. Compared to the other sensors, fiber optic sensors (FOSs) based on optical fiber sensing technology have attracted increasing attentions due to the unique advantages, such as anti-electromagnetic, compactness, high sensitivity and so on.

FOSs can be used to monitor and measure the external physical variables, including temperature [1]–[3], strain [4], [5],

Xuekai Gao, Jian Xu, Caijian Xie, Li Pei, Jingjing Zheng, Jing Li, and Tigang Ning are with the Key Lab of All Optical Network & Advanced Telecommunication Network of EMC, Institute of Lightwave Technology, Beijing Jiaotong University, Beijing 100044, China (e-mail: 16111006@bjtu.edu.cn; 19111041@bjtu.edu.cn; cj_xie@bjtu.edu.cn; lipei@bjtu.edu.cn; jjzheng@bjtu.edu.cn; lijing@bjtu.edu.cn; tgning@bjtu.edu.cn).

Wei Zhang is with the Beijing Institute of Spacecraft Environment Engineering, Beijing 100094, China (e-mail: feeling5404@163.com).

refractive index (RI) [6]–[8], liquid level [9]–[11], magnetic field [12], [13], humidity [14], [15]. Temperature is a significant physical quantity because many physical phenomena and chemical processes are carried out at a certain temperature. Production processes, mechanical operation, and living environment call for specific temperatures. Therefore, temperature measuring is an essential procedure to ensure the security of production and people living [16]. With the rapid development of science and technology, higher requirements are put forward for temperature measurement. Fiber temperature sensing technology can be applied to measure or monitor the changes in temperature, which is one of the important application directions for FOSs[17]. There is a wide range of high-performance fiber temperature sensors, but many of these sensors still suffer from cross-sensitivity between temperature and the other physical quantities. Thus, a lot of novel fiber sensor structures are proposed to tackle this issue. In 2014, Zhigang Cao *et al.* proposed a strain-insensitive and high-temperature fiber sensor. The proposed fiber sensor is composed of a piece of small-core photo-sensitive fiber (SCPSF), which is spliced to the single mode fiber (SMF) with the core-offset at the spliced position [18]. The temperature sensitivity of the sensor is 106.64 pm/°C from 200 °C to 1000 °C, and the temperature to strain cross sensitivity of the sensor is low as 0.00675 °C/$\mu\varepsilon$. In 2017, Yu *et al.* demonstrated a fiber optic sensor for simultaneous temperature and strain monitoring based on a few-mode solid-core photonic crystal fiber. The temperature and strain sensitivities of the fiber sensor are 9.85 pm/°C and 3.24 pm/$\mu\varepsilon$ respectively [19]. In 2018, Zhang *et al.* suggested a novel SMF-based up taper-down taper-up taper (UDU) structure based on miniaturized modal interferometer (MMI) for simultaneous RI, strain, and temperature measurement, achieving a RI sensitivity of 131.93 nm/RIU, a strain sensitivity of 0.0007 nm/$\mu\varepsilon$, and a temperature sensitivity of 87.8 pm/°C respectively [20]. In 2019, Song *et al.* designed and tested a strain-insensitive fiber temperature sensor by employing a DNA-CTMA (DNA-Cetyl trimethyl ammonium) solid film coated on micro-tapered fiber [21], obtaining temperature sensitivity of -900 pm/°C in the bio-medical temperature region and a very low strain sensitivity of -7 pm/$\mu\varepsilon$. In 2020, Tong Nan *et al.* proposed a temperature sensor constructed by fusion splicing a piece of suspended-core microstructure optical fiber (SCMF) between two up-tapers, achieving The sensitivity of -0.011 rad/°C in the temperature range of 20°C to 90°C [22]. In the same year, Lee *et al.* proposed a strain-insensitive fiber-type temperature sensor based on dense microscale wrinkles on the fiber surface[23]. Most of these FOSs are designed by utilizing core offset, tapering, and other special
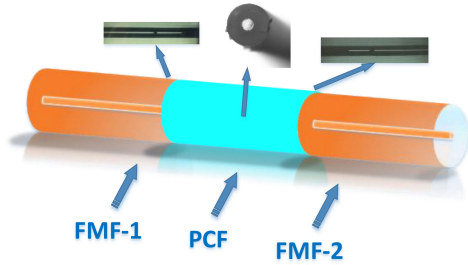
Fig. 1.   Schematic diagram of the sensor structure.

Fig. 2.   (a) The cross-section diagram of FMF. (b) The cross-section diagram of PCF.

techniques to ensure high sensing performances. However, the manufacturing processes of those special structures are difficult to manage precisely because the fabrication process for these sensors is sophisticated, which can degrade the sensing performances. For example, sensitivity can decrease when there is slight deviation from the specially designated degree of the fiber taper or core-offset. Therefore, it is necessary to take into account the engineering fabrication difficulty when designing the fiber sensor.

We propose a fiber temperature sensor composed of the few-mode fiber (FMF) and photonic crystal fiber (PCF) in this paper. The proposed sensor has an FMF-PCF-FMF-based hybrid structure that can be easily achieved by directly splicing the FMF and PCF. There are resonant peaks in the transmission spectrum when the mode interference occurs in the FMF-PCF-FMF structure, and the resonant peaks shift as the temperature changes. Thus, temperature variation can be measured by monitoring shift of resonant peaks. Experimental results indicate that the proposed fiber sensor not only has a high temperature sensitivity of 38.6 pm/°C but also has a low axial strain response, which illustrates that the proposed sensor solves the issue of cross-sensitivity effectively. Furthermore, the proposed fiber temperature sensor has the advantage of being sturdy and easy to use compared to those sensors proposed in [18]–[21], improving its engineering practicality and flexibility.

II. SENSING PRINCIPLE

Fig. 1 depicts a schematic design of the proposed sensor structure. The sensor consists of two pieces of FMF and one pieces of PCF. After manual alignment, the two ends of a short piece of the PCF (YOFC) are fused with two FMFs that support the modes LP_{01}, LP_{11}, LP_{21}, and LP_{02}. And the refractive index of core and cladding of FMF are 1.46111 and 1.45601, respectively. The FMF has a core diameter of 18 μm and a cladding diameter of 125 μm. The refractive index of PCF is 1.4625. The PCF have a cladding diameter of 125 μm and an air hole diameter of 3 μm. The fabrication of the proposed sensor does not include splicing methods such as offset splicing, tapering, etc. Thus, the structure of the proposed sensor can be completed by the auto splicing program of the Fiber Fusion Splicer, which avoids the splicing error caused by manual splicing and greatly improves the reproducibility of manufacturing of this type of sensor. The sensor has a symmetrical structure that ensures it is independent of access direction, making it extremely practical to use. The
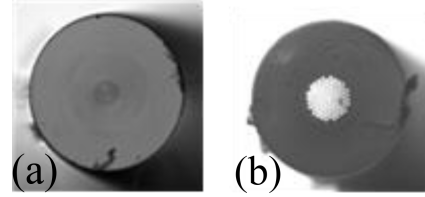
FMF-1 serves as a beam splitter, while the FMF-2 serves as a combiner. Fig. 1 shows a micrograph of the splicing. The sensor's manufacturing is straightforward. The cross-section of the fiber of FMF and PCF is shown in Fig. 2.

Lead-in and lead-out SMFs are spliced into the two ends of the FMF-PCF-FMF sensor. When light passes through the FMF-PCF-FMF, modal interference occurs between the fundamental mode and the cladding modes because core and cladding modes have different effective refractive indexes. The phase difference $\Delta\varphi$ between the fundamental mode and the cladding modes is dependent on the effective refractive index, and given by [24]:

$$\Delta\varphi = \frac{2\pi L \Delta n_{eff}}{\lambda}, \tag{1}$$

where L denotes the sensor length and λ is the wavelength of light in a vacuum. The effective refractive index difference between the fundamental mode and the cladding modes is Δn_{eff}. When the phase difference matches the condition $\Delta\varphi = (2k+1)\pi$, the wavelength of the resonant peak λ_k can be expressed as [24]:

$$\lambda_k = \frac{2}{2k+1}\Delta n_{eff}L, \tag{2}$$

where k is an integer.

Owing to the thermal expansion effect and the thermo-optic effect, the geometric size and refractive index of the fiber change with different temperature, resulting in the wavelength shift of resonant peaks [16]. The wavelength shift induced by temperature changes can thus be calculated by [25]

$$\frac{\Delta\lambda}{\lambda_k} = [\alpha + \xi]\Delta T, \tag{3}$$

where ΔT denotes temperature change, while α and ξ denote thermal expansion coefficient and thermo-optic coefficient, respectively.

The wavelength can also shift when strain is applied to the fiber sensor and the sensor geometry changes in fiber dimensions due to the photo-elastic effect [26]. The wavelength shift induced by strain can be calculated by [27].

$$\frac{\Delta\lambda}{\lambda_k} = \left[1 + \frac{L}{\Delta n_{eff}}\cdot\frac{\partial\left(\Delta n_{eff}\right)}{\partial L}\right]\Delta\varepsilon = (1+P_e)\Delta\varepsilon \tag{4}$$

where P_e is the effective photo-elastic coefficient and $\Delta\varepsilon$ represents the change in strain.

Transmission spectrum of the sensor can be simulated by using the beam propagation method (BPM). The core and cladding diameters of FMFs are 18 μm and 125 μm respectively, while the refractive indexes of the core and cladding are 1.45601 and
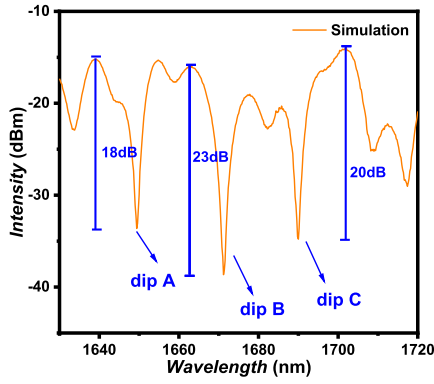
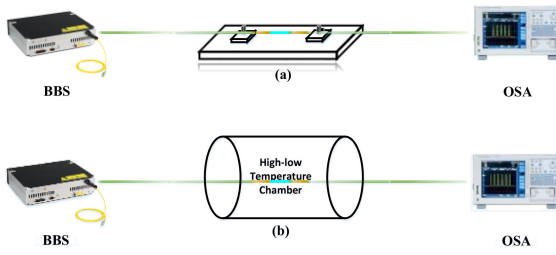Fig. 3.   The simulation spectrum of the structure.

Fig. 4.   (a) Schematic diagram of the strain experimental setup. (b) Schematic diagram of the temperature experimental setup.

Fig. 5.   (a) The transmission spectrum and (b) the spatial frequency spectrum of the proposed sensor.

1.46111. The diameter of the PCF is 125 μm, and the cladding has a refractive index of 1.4625 while the air hole has a refractive index of 1. The length of the PCF employed in the simulation is 1 cm, and the length of the two pieces FMFs is 2 cm. The simulation spectrum of the fiber sensor is shown in Fig. 3. There are three resonant peaks in the wavelength between 1630 nm and 1720 nm. Dip A has an extinction ratio of roughly 18 dB at the wavelength of 1649.4 nm. At the wavelength of 1671.2 nm, dip B has an extinction ratio of roughly 23 dB. Dip C has an extinction ratio of around 20 dB at the wavelength of 1690 nm. Temperature changes can be measured by the wavelength shifts of the dips A, B, and C.

III. EXPERIMENT

The experimental setup of the sensor under strain and temperature measurement is shown in Fig. 4. The light from a broadband light source (BBS, YLS SC-5) is launched into the sensor that is imposed strain or temperature. The optical spectrum of modulated light signals from the sensor can be obtained through an optical spectrum analyzer (OSA, YOKOGAWA AQ6375). We measured the spectrum of the sensor under initial state, and the transmission spectrum of the sensor under room temperature of 20 °C and strain of 0 $\mu\varepsilon$ is depicted in Fig. 5(a). The spectrum shows multiple resonant peaks in the wavelength region of 1630 to 1720 nm. There are three resonant peaks and dips, which is in agreement with the simulated results shown in Fig.3. At the wavelength of 1642 nm, dip A has an extinction ratio of about 17 dB. At the wavelength of 1675 nm, dip B has an extinction ratio of roughly 15 dB. Dip C has an extinction ratio of roughly
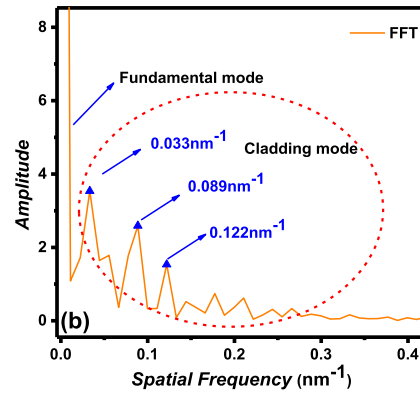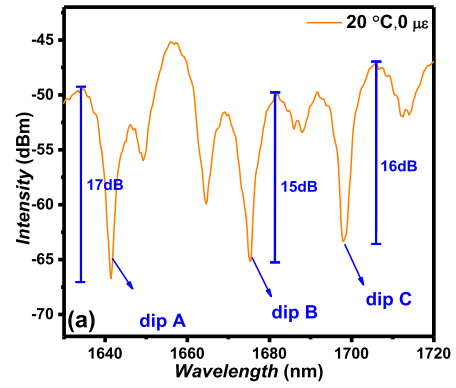
16 dB at the wavelength of 1699 nm. Compared with the simulated results in the Fig.3, the experimental spectrum exhibits a higher power loss than the simulation spectrum, and there is a slight discrepancy in the wavelength of the interference peak. It can be attributed to the fact that there is power loss induced by the fiber fusion for the sensor, resulting in the above-mentioned disparities. Wavelengths of Dips A, B, and C will shift when the sensor is imposed external temperature and strain, which can be measured by OSA.

The spatial frequency spectrum of the transmission spectrum is derived by using the Fast Fourier Transformation (FFT), as shown in Fig. 5(b). The fundamental mode is the dominating peak in the spatial frequency spectrum, and there are three cladding modes at 0.033 nm^{-1}, 0.089 nm^{-1}, and 0.122 nm^{-1}. In addition, there are more peaks with lower amplitude intensities [28]. The relationship between spatial frequency ξ and the effective refractive index difference Δn_{eff} is given by [29]:

$$\Delta n_{eff} = \lambda^2 \xi / 2L \tag{5}$$

where L and λ are the length and the center wavelength of the sensor. The Δn_{eff} is calculated to be the 10^{-4} order of magnitude at the peak of 0.033 nm^{-1}. The Δn_{eff} is calculated to be the 10^{-3} order of magnitude at the peak of 0.089 nm^{-1}. The Δn_{eff} is calculated to be at 10^{-3} orders of magnitude at the

peak of $0.122 \, \mathrm{nm}^{-1}$. Those effective refractive index differences are almost the same as the refractive index difference between core and cladding in the Reference [30].

Two ends of the sensor are clamped by a stationary stage and a translation stage in the experiment to detect strain. At room temperature, the strain can be modified by altering the distance between the fixed stage and the translation stage. In the experiment, the length of the sensor increases 0.03 mm as the sensor is stretched once, and the step of the imposed strain is set as 600 $\mu\varepsilon$. The transmission spectra of dips A, B, and C under strain of 0, 600, 1200, 1800, 2400, and 3000 $\mu\varepsilon$ are shown in Fig. 6(a), (b), and (c), respectively. The wavelengths of the dips A, B, and C shift slightly towards the shorter wavelength as the strain increases. In the range of 0 to 3000 $\mu\varepsilon$, the wavelength shifts of dip A, B, and C are −1.6 nm, −1.4 nm, and −1.6 nm, respectively. Linear fitting curves of wavelength shift for dips A, B, and C under increasing strain are represented in Fig. 6(d). The red line, blue line, and orange line denote the wavelength shifts for dips A, B, and C respectively. According to the linear fitting curves, the strain sensitivities of the dips A, B, and C in the range of 0 to 3000 $\mu\varepsilon$ are −0.457 pm/$\mu\varepsilon$, −0.495 pm/$\mu\varepsilon$, and −0.53 pm/$\mu\varepsilon$, respectively. The three dips present the very low strain sensitivities in the wide range of strain, which indicates the proposed sensor is insensitive to the strain. Moreover, we find the depth and width variations of resonating dips with the changing of strain. The reason for this phenomenon is that the length of the sensor will increase when the strain increases and the refractive index difference between the core and the cladding decrease as the strain increases. The changes in the fiber length and the refractive index difference can cause the change of phase difference between the core mode and cladding mode of optical fiber, which will lead to the change in interference spectrum. Thus, the extinction ratio and the spectral width of resonating dips slightly fluctuate [31], [32].

For the temperature sensing experiment, the sensor is placed in the Weiss WTI-180/40 High-Low Temperature Chamber, which has a temperature resolution of 1 °C. In the experiment, the temperature increases from 20 °C to 80 °C, and the transmission spectra at 20, 30, 40, 50, 60, 70, and 80 °C are shown in Fig. 7(a), (b), and (c), the wavelengths of the dips A, B, and C shift to the longer wavelength as the temperature increases, as illustrated in Fig. 7(a), (b), and (c). In the region of 20 to 80°C, the wavelength of dip A, B, and C shift 1.8 nm, 2.2 nm, and 2 nm, respectively. Based on the wavelength shifts at 20, 30, 40, 50, 60, 70, and 80 °C, temperature sensitivity can be calculated by linear fitting. The orange, red, and blue lines in Fig. 7(d) represent linear fitting curves of dip A, B, and C with increasing temperature, respectively. According to the linear fitting results, the temperature sensitivities of the dips A, B, and C in the range of 20 to 80 °C are 30 pm/°C, 38.6 pm/°C, and 35.7 pm/°C, respectively. Thus, the dip B present the highest temperature response. These high temperature sensitivities suggest that the proposed sensor is very sensitive the temperature change, which can be applied to temperature measurement. In the temperature measurement experiment, owing to the thermal expansion effect and the thermo-optic effect, there also is depth and width
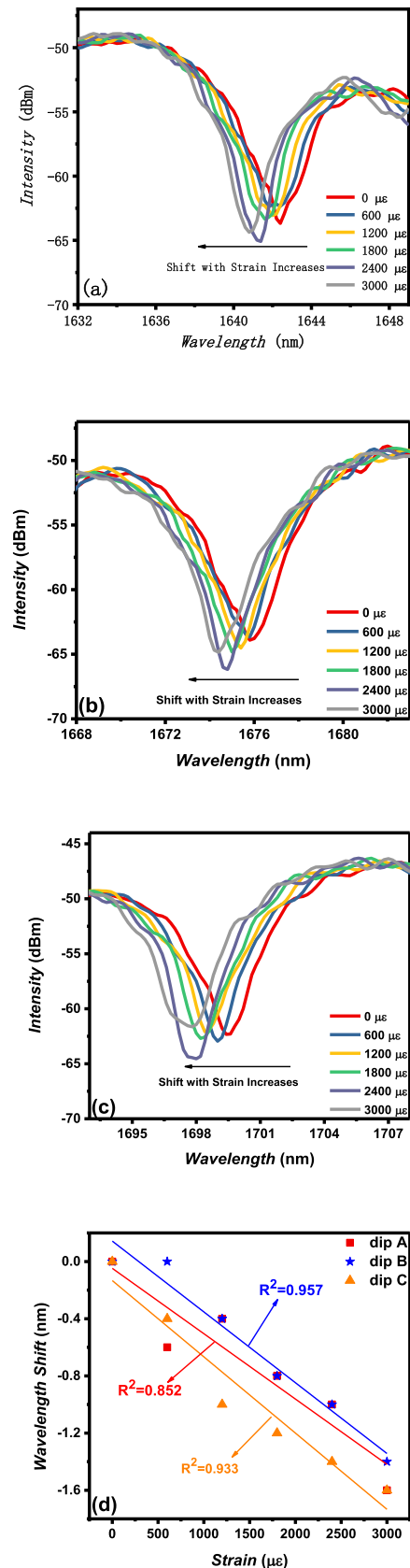

Fig. 6. (a), (b), and (c) The transmission spectra of the dip A, B, and C under increasing strain from 0 to 3000 $\mu\varepsilon$, respectively. (d) The linear fitting of the sensor with increasing strain.

Fig. 8. (a) The spatial frequency spectrum response in the range from 20 to 80 °C. Inset: The corresponding zoom images. (b) The linear fit of the sensor with increasing temperature.
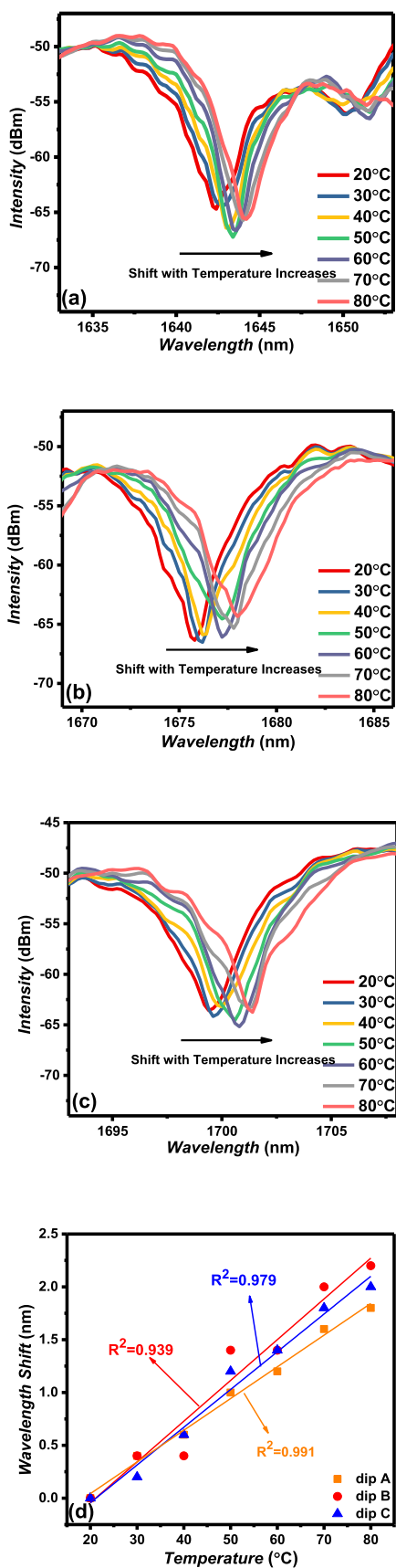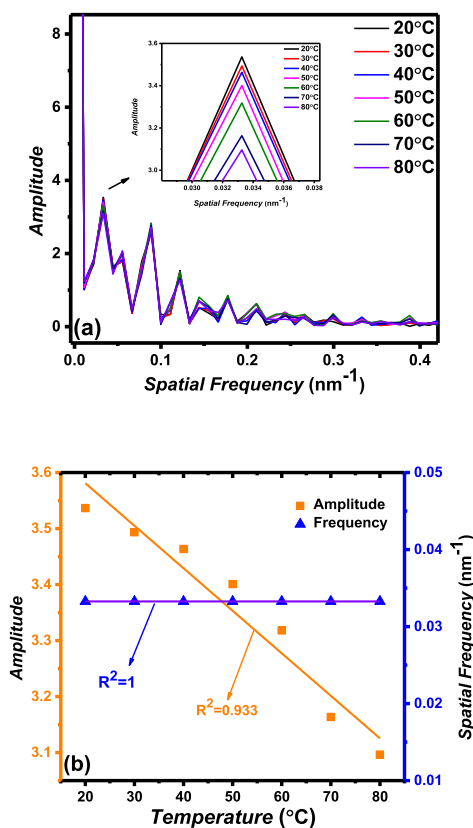

Fig. 7. (a), (b), and (c) The transmission spectra of the dip A, B, and C with increasing temperatures from 20 to 80 °C, respectively. (d) The linear fitting of the sensor with increasing temperature.

variations of resonating dips under different temperatures. This is because the geometric size and refractive index of the fibers vary when the response temperature varies. The changes in the geometric size and refractive index of fibers have impacts on the mode interference effect, which results in depth and width variations of resonating dips.

According to Fig.7, the largest temperature sensitivity is 38.6 pm/°C. The dip wavelength shift under per unit temperature can be measured when the resolution of the optical spectrum analyzer is higher than 38.6 pm. In other words, the quality of this measurement can be improved by the optical spectrum analyzer with a higher resolution. For example, the dip wavelength shift as the temperature increases 0.5°C can be measured by the optical spectrum analyzer with a resolution of 19.3 pm. In application, it can be found the slight fluctuation of the transmission spectrum when the data is obtained at a smaller sampling interval. In order to obtain a more accurate dip wavelength, a demodulator can be applied in the specific measurement. Thus, employing the demodulator also is an important method to improve the quality of the measurement.

In order to further investigate performances of the proposed sensor, the transmission spectrum as a function of temperature can be analyzed by the amplitude of the spatial frequency spectra as referring to [25]. Fig. 8(a) depicts the spatial frequency spectrum of the sensor under temperatures of 20, 30,

TABLE I
COMPARISON OF SENSITIVITY OF THE FIBER SENSORS

Structures of sensors	$\mathbf{pm}$/°C(range)	$\mathbf{pm}/\boldsymbol{\mu\varepsilon}$(range)
Few-mode PCF [19]	9.85(20-60 °C)	3.24(0-541.2με)
Few-mode PCF [33]	1.66(20-60 °C)	2.74(0-420 με)
Cascaded Two-Core PCFs[34]	9.7(20-350 °C)	1.86(0-3600 με)
The proposed sensor	38.6(20-80 °C)	-0.457(0-3000με)

40, 50, 60, 70, and 80 °C. At the spatial frequency of 0.033 nm^{-1}, the amplitude the spatial frequency decreases from 3.54 to 3.1 when the temperature increases from 20 to 80 °C, which can be used to analyze temperature change more simply and intuitively. In Fig. 8(b), the orange and bule lines denote the changes of the amplitude and spatial frequency, respectively. There is a strong linear match between amplitude and temperature, and the temperature sensitivity is 0.00759 a.u./°C according to the amplitude changes induced by temperature changes. Furthermore, the stable blue line indicates an excellent linear fit between the spatial frequency and temperature, which suggests that the spatial frequency keeps stable. From the above analysis, temperature sensitivity of temperature sensor can also be analyzed accurately by the spatial frequency spectra.

The temperature resolution in the region of 20 to 80 °C is 1.25 °C based on the wavelength resolution of 50 pm of the optical spectrum analyzer and the temperature sensitivity of 38.6 pm/°C of the dip B. Table I makes comparison between the proposed fiber sensor and fiber sensors with other structures based on PCFs. The wavelength shift of 38.6 pm is much greater than 9.85, 1.66, and 9.7 pm for the fiber temperature sensors proposed in Refs. [19], [33], and [34], as illustrated in Table I. Therefore, the fiber temperature sensor proposed in this paper represents higher responsiveness, which also reduces the demand for the resolution of the optical spectrum analyzer. Results suggest that the proposed fiber sensor not only has a high temperature sensitivity but also has a lower strain sensitivity compared to the other similar fiber sensors, which indicates the proposed sensor can solve the cross-sensitivity to a certain extent.

IV. CONCLUSION

In conclusion, we design and experimentally demonstrate a novel strain-insensitive temperature sensor composed of FMF and PCF. The sensor is an FMF-PCF-FMF hybrid construction, and the symmetrical structure makes the sensor be independent of light inject direction, ensuring that it is extremely practical to use. Experimental results suggest that the temperature sensitivity of the proposed fiber sensor is high as 38.6 pm/°C when the temperature ranging from 20 to 80 °C, and the temperature sensitivity is 0.00759 a.u./°C by evaluating the amplitude of the spatial frequency spectrum. Meanwhile, the sensor has a strain sensitivity of -0.457 pm/$\mu\varepsilon$ in the range of 0 to 3000 $\mu\varepsilon$, showing insensitive to strain. Furthermore, the proposed sensor structure is compact, and the fabrication is simple and easy. The advantages of high temperature sensitivity, ultralow strain sensitivity, and convenient fabrication make the proposed sensor be applied for sensing applications.

REFERENCES

[1] X. Yu, S. Wang, J. F. Jiang, K. Liu, Z. Y. Wu, and T. G. Liu, "Self-filtering high-resolution dual-sapphire-fiber-based high-temperature sensor," *J. Lightw. Technol.*, vol. 37, no. 4, pp. 1408–1414, Feb. 2019.

[2] Y. Wu *et al.*, "High sensitivity micro-fiber Mach-Zehnder interferometric temperature sensors with a high index ring layer," *Opt. Exp.*, vol. 27, no. 23, pp. 34247–34257, 2019.

[3] C. E. Dominguez-Flores *et al.*, "Real-time temperature sensor based on in-fiber Fabry–Perot interferometer embedded in a resin," *J. Lightw. Technol.*, vol. 37, no. 4, pp. 1084–1090, Feb. 2019.

[4] J. Tian, Z. Li, Y. Sun, and Y. Yao, "High-sensitivity fiber-optic strain sensor based on the vernier effect and separated Fabry–Perot interferometers," *J. Lightw. Technol.*, vol. 37, no. 21, pp. 5609–5618, Nov. 2019.

[5] C. Lang, Y. Liu, K. Cao, and S. Qu, "Temperature-insensitive optical fiber strain sensor with ultra-low detection limit based on capillary-taper temperature compensation structure," *Opt. Exp.*, vol. 26, no. 1, pp. 477–487, Jan. 2018.

[6] F. Yu, P. Xue, and J. Zheng, "Study of a large lateral core-offset in-line fiber modal interferometer for refractive index sensing," *Opt. Fiber Technol.*, vol. 47, pp. 107–112, Jan. 2019.

[7] F. Yu, P. Xue, and J. Zheng, "Enhancement of refractive index sensitivity by bending a core-offset in-line fiber Mach-Zehnder interferometer," *IEEE Sensors J.*, vol. 19, no. 9, pp. 3328–3334, May 2019.

[8] M. Yang *et al.*, "Refractive index sensor based on etched eccentric core few-mode fiber dual-mode interferometer," *Opt. Exp.*, vol. 27, no. 20, pp. 28104–28113, Sep. 2019.

[9] D. Liu *et al.*, "Sub-micrometer resolution liquid level sensor based on a hollow core fiber structure," *Opt. Lett.*, vol. 44, no. 8, pp. 2125–2128, Apr. 2019.

[10] C. Sun, Y. Dong, M. Wang, and S. Jian, "Liquid level and temperature sensing by using dual-wavelength fiber laser based on multimode interferometer and FBG in parallel," *Opt. Fiber Technol.*, vol. 41, pp. 212–216, Mar. 2018.

[11] B. Preloznik, D. Gleich, and D. Donlagic, "All-fiber, thermo-optic liquid level sensor," *Opt. Exp.*, vol. 26, no. 18, pp. 23518–23533, Sep. 2018.

[12] R. Zhang *et al.*, "Mach-Zehnder interferometer cascaded with FBG for simultaneous measurement of magnetic field and temperature," *IEEE Sensors J.*, vol. 19, no. 11, pp. 4079–4083, Jun. 2019.

[13] G. Wang, Y. Lu, X. Yang, L. Duan, and J. Yao, "High-sensitivity magnetic field sensor based on a dual-core photonic crystal fiber," *Appl. Opt.*, vol. 58, no. 21, pp. 5800–5806, Jul. 2019.

[14] X. Wang, K. Tian, L. Yuan, E. Lewis, G. Farrell, and P. Wang, "A high-temperature humidity sensor based on a singlemode-side polished multimode-singlemode fiber structure," *J. Lightw. Technol.*, vol. 36, no. 13, pp. 2730–2736, Jul. 2018.

[15] K. P. W. Dissanayake, W. P. Wu, H. Nguyen, T. Sun, and K. T. V. Grattan, "Graphene-oxide-coated long-period grating-based fiber optic sensor for relative humidity and external refractive index," *J. Lightw. Technol.*, vol. 36, no. 4, pp. 1145–1151, Feb. 2018.

[16] X. Gao *et al.*, "Simultaneous measurement of refractive index, strain, and temperature based on a Mach–Zehnder interferometer with hybrid structure optical fiber," *Appl. Opt.*, vol. 58, no. 30, pp. 8187–8193, 2019.

[17] R. Bogue, "Fibre optic sensors: A review of today's applications," *Sensor Rev.*, vol. 31, no. 4, pp. 304–309, 2011.

[18] Z. Cao *et al.*, "Strain-insensitive and high temperature fiber sensor based on a Mach–Zehnder modal interferometer," *Opt. Fiber Technol.*, vol. 20, no. 1, pp. 24–27, 2014.

[19] H. Yu, Z. Zheng, J. Ma, Y. Zheng, M. Yang, and X. Jiang, "Temperature and strain sensor based on a few-mode photonic crystal fiber," in *Proc. IEEE Sensors*, 2017, pp. 1–3.

[20] N. Zhang *et al.*, "Simultaneous measurement of refractive index, strain and temperature using a tapered structure based on SMF," *Opt. Commun.*, vol. 410, pp. 70–74, 2018.

[21] S. Song, A. Jung, S. Hong, and K. Oh, "Strain-Insensitive biocompatible temperature sensor based on DNA solid film on an optical microfiber," *IEEE Photon. Technol. Lett.*, vol. 31, no. 24, pp. 1925–1928, Dec. 2019.

[22] T. Nan *et al.*, "Optical fiber temperature sensor with insensitive refractive index and strain based on phase demodulation," *Microw. Opt. Technol. Lett.*, vol. 62, pp. 3733–3738, 2020.

[23] J. Lee *et al.*, "Intrinsically strain-insensitive, hyperelastic temperature-sensing fiber with compressed micro-wrinkles for integrated textronics," *Adv. Mater. Technol.*, vol. 5, 2020, Art. no. 2000073.

[24] X. Dong, H. Du, X. Sun, and J. Duan, "Simultaneous strain and temperature sensor based on a fiber Mach-Zehnder interferometer coated with Pt by iron sputtering technology," *Materials*, vol. 11, no. 9, Aug. 2018, Art. no. 1535.

[25] C. Zhang *et al.*, "Miniature optical fiber temperature sensor based on FMF-SCF structure," *Opt. Fiber Technol.*, vol. 41, pp. 217–221, Mar. 2018.

[26] A. Kumar, N. K. Goel, and R. K. Varshney, "Studies on a few-mode fiber-optic strain sensor based on LP01-LP 02 mode interference," *J. Lightw. Technol.*, vol. 19, no. 3, pp. 358–362, Mar. 2001.

[27] J. Zheng *et al.*, "Temperature and index insensitive strain sensor based on a photonic crystal fiber in line Mach–Zehnder interferometer," *Opt. Commun.*, vol. 297, pp. 7–11, 2013.

[28] J. Liu, X. Liang, C. Sun, and S. Jian, "Fiber ring laser for axial micro-strain measurement by employing few-mode concentric ring core fiber," *Opt. Fiber Technol.*, vol. 33, pp. 16–21, Jan. 2017.

[29] L. Duan *et al.*, "Heterogeneous all-solid multicore fiber based multipath Michelson interferometer for high temperature sensing," *Opt. Exp.*, vol. 24, no. 18, pp. 20210–20218, 2016.

[30] X. Gao *et al.*, "A dual-parameter fiber sensor based on few-mode fiber and fiber Bragg grating for strain and temperature sensing," *Opt. Commun.*, vol. 454, 2020, Art. no. 124441.

[31] X. Gao *et al.*, "Simultaneous measurement of strain and temperature based on no-core fiber and two-core fiber," *Sensor Actuat A-Phys. Rev.*, vol. 331, 2021, Art. no. 113013.

[32] L. Li, L. Xia, Z. Xie, and D. Liu, "All-fiber Mach-Zehnder interferometers for sensing applications," *Opt. Exp.*, vol. 20, no. 10, pp. 11109–11120, May 2012.

[33] Z. Z. Luo, H. H. Yu, Y. Zheng, Z. Zheng, Y. J. Li, and X. Jiang, "Selective mode excitation in a few-mode photonic crystal fiber for strain sensing with restrained temperature response," *J. Lightw. Technol.*, vol. 38, no. 16, pp. 4560–4571, Aug. 2020.

[34] K. Naeem, Y. Chung, and B. H. Kim, "Cascaded two-core PCFs-based in-line fiber interferometer for simultaneous measurement of strain and temperature," *IEEE Sensors J.*, vol. 19, no. 9, pp. 3322–3327, May 2019.